Bulletin of the Seismological Society of America, 89, 3, pp. 608–625, June 1999

Generic Finite-Fault Model for Ground-Motion Prediction in Eastern North America

by Igor A. Beresnev and Gail M. Atkinson

Abstract Ground-motion models based on the Brune point-source approximation have an underlying ω^2 spectrum, with a single corner frequency. These models overpredict observed spectral amplitudes at low to intermediate frequencies (~0.1 to 2 Hz), for earthquakes with moment magnitudes M of 4 or greater. The empirical spectra of moderate to large events tend to sag at these frequencies, relative to the level suggested by the Brune point-source model.

A model that accounts for the finite extent of the fault plane correctly describes the observed spectral shapes. The model represents seismic radiation as a sum of contributions from several subfaults. Each subfault may be represented as a point source, and each subevent has an ω^2 spectrum. When contributions to ground motion at an observation point are summed over all subfaults, the resulting spectral shape has two corner frequencies and more closely matches observed spectra. The more realistic spectral shape obtained through finite-fault modeling reflects the underlying reality that the radiation from real faults is formed by ruptures of their smaller parts, whose corner frequencies are higher than those implied by the full fault dimension. The two corners appear naturally as a result of subevent summation.

We use the stochastic finite-fault methodology to simulate the recorded ground-motion data from all significant earthquakes in eastern North America (ENA). These data include eight events of $M > 4$ recorded on modern digital instruments (regional seismographs and strong-motion instruments), and three historical events of M 5.8 to 7.3 recorded on analog instruments. The goodness of fit of synthetics to the data is defined as simulation bias, which is indicated by the difference between the logarithms of the observed and the simulated spectrum, averaged over all recordings of an earthquake. The finite-fault simulations provide an unbiased fit to the observational database over a broad frequency range (0.1 to 50 Hz), for all events.

A surprising conclusion of these simulations is that the subfault size that best fits the observed spectral shape increases linearly with moment magnitude, in an apparently deterministic manner. This strongly suggests that the subfault size can be unambiguously defined by the magnitude of the simulated earthquake. In this case, the radiation-strength factor(s), which is proportional to the square root of the high-frequency Fourier acceleration level, remains the only free parameter of the model. Its value is related to the maximum slip velocity on the fault. The strength factors for all modeled ENA events are within the range of 1.0 to 1.6, with the exception of the Saguenay mainshock ($s = 2.2$). This suggests a remarkable uniformity in earthquake slip processes.

Introduction

It has been shown that the use of a Brune point-source spectrum, in conjunction with a stochastic ground-motion model, successfully predicts *high-frequency* ($f \geqq 2$ Hz) ground-motion amplitudes for earthquakes in California (Hanks and McGuire, 1981; Boore, 1983) and eastern North America (ENA) (Atkinson, 1984; Boore and Atkinson, 1987; Toro *et al.*, 1997). The underlying spectrum of ground acceleration for this model has a simple ω^2 shape, meaning that the spectral amplitudes decay as ω^{-2}, for frequencies below the corner frequency, where the corner frequency is a function of magnitude. Despite its success in modeling high-frequency motions, the Brune point source consistently

overpredicts seismic motions from significant (moment magnitude $M > 4$) earthquakes at low to intermediate frequencies (~0.1 to 2 Hz), both in eastern North America and California (Boatwright and Choy, 1992; Boore and Atkinson, 1992; Atkinson, 1993a; Atkinson and Boore, 1995; Atkinson and Silva, 1997). To account for the observed lack of energy at intermediate frequencies, relative to the single-corner model, Atkinson (1993a) proposed an empirical source spectrum with two corner frequencies, representing an addition of Brune point-source spectra. This two-corner point-source model was then used to develop stochastic ground-motion relations for eastern North America (Atkinson and Boore, 1995). These relations are in demonstrably better agreement with empirical data than are relations based on a single-corner-frequency model (Atkinson and Boore, 1998).

Atkinson and Silva (1997) showed that finite-source effects could be the reason for the observed discrepancy between single-corner point-source simulations and empirical data. They compared empirical source spectra for California earthquakes with the predictions of both single-corner-frequency point-source and stochastic finite-fault simulations. In their finite-fault simulations, the fault was subdivided into a number of subfaults, each of which was modeled as a Brune point source. The spectral shape from the finite-fault modeling matched the observed spectra, as the summation over a number of Brune sources reproduced the observed spectral sag at intermediate frequencies. By contrast, the single-corner point-source model could not provide a satisfactory match to the observed spectra.

In this article, we use the stochastic finite-fault methodology of Beresnev and Atkinson (1997, 1998a) to model the ground motions from all ENA mainshock or foreshock earthquakes of $M > 4$ that have been recorded digitally or in analog form. We show that this model reproduces the salient ground-motion characteristics of all events. The data set is comprised of eight digitally recorded recent events and three historic earthquakes, providing comparisons between synthetic and empirical data in the magnitude range from 4.2 to 7.3, over the frequency band from 0.1 to 50 Hz.

Earthquake Data

Table 1 provides a list of modeled events in order of increasing moment magnitude, with references to studies from which the fault parameters and characteristics of ground motions were extracted. Table 2 lists all digital, strong-motion, and historic seismograph stations used in the analyses. All stations are founded on rock.

In comparing the results of simulations with observations, we use the empirical ENA response spectra database compiled by Atkinson and Boore (1998). It is comprised of horizontal response spectra computed from 221 individual recordings on rock sites for all significant recorded ENA events. Spectra are tabulated at frequencies of 0.1, 0.2, 0.5, 1, 2, 5, and 10 Hz (to the extent that this is allowed by the useable passband of the recording instruments). For stations that have no recorded horizontal component, the database lists horizontal spectral values converted from the vertical component using the empirical relation of Atkinson (1993b). Where the recorded data from two horizontal components are available, we take their arithmetic average.

Figure 1 shows the locations of earthquake epicenters and recording stations. Ten events are plotted, with the Saguenay mainshock and its foreshock indicated as one symbol. The 1985 Nahanni event occurred in the Northwest Territories, near the western edge of the Canadian shield, approximately 2500 km to the northwest of the map area; however, tectonically, it is considered an intraplate event (Wetmiller *et al.*, 1988). The densely instrumented Charlevoix Seismic Zone area is outlined by a rectangle in Figure 1, with its blowup view provided in Figure 2.

Finite-Fault Simulation Method

All simulations are carried out using the computer program FINSIM, which combines the stochastic ground-motion modeling technique with the kinematic model of rupture propagation. An earthquake fault is discretized as an array of subfaults, each of which is modeled as a stochastic ω^2 point source. Each subfault is triggered when the rupture front reaches it. The ground motion at an observation point is obtained by summing contributions over all subfaults. A complete description of the method and the code is provided by Beresnev and Atkinson (1997, 1998a). Stochastic simulations provide a random horizontal component of ground motion. Three trials of the stochastic simulation are used to estimate an average response spectrum at each site.

The way the earthquake radiation is represented in the finite-fault model explains why it reproduces the observed spectral sag that is missed by the Brune point-source model. The central idea of kinematic modeling is the discretization of a large fault plane into elements (subfaults), each of which is assigned a corner frequency inversely proportional to its size. The total radiation is then obtained by summing contributions from all subfaults. In the Brune point-source approximation, the corner frequency of a large fault is derived from the full fault dimension, and is thus much lower than that of the subfaults. Figure 3 illustrates the difference in total radiation that occurs. For the same high-frequency spectral level, the spectrum given by the finite-fault approximation starts to decay at frequencies around the subsource corner frequency (f_{0H}), where the point-source spectrum is still flat. However, both spectra are constrained by the same total moment, which forces them to converge at the low-frequency end. Thus, the finite-source spectrum necessarily acquires the second, low-frequency corner (f_{0L}), and the sag appears. Each subfault still has a single-corner-frequency spectrum; the sag is automatically created by the summation procedure that prescribes the high-frequency level and the

Table 1
Event and Finite-Fault Modeling Parameters

Event Name	Date	Epicenter Coordinates (deg)	Moment Magnitude	Strike and Dip (deg)	Depth to Upper Edge (km)	Number of Stations	References*	Fault Dimensions Along Strike and Dip (km)	Subfault Size (km)	Radiation-Strength Factor
Cap Rouge, Québec	11/05/97	46.79, −71.40	4.2	49, 71	22	22	Nadeau *et al.* (1998), http://www.seismo.nrcan.gc.ca/	1 × 1	0.5	1.6
Saguenay foreshock, Québec	11/23/88	48.13, −71.20	4.2	333, 51	29	10	Adams (1995), AB98‡	1 × 1	0.5	1.0
Mont Laurier, Québec	10/19/90	46.47, −75.59	4.5	276, 70	11	11	Lamontagne *et al.* (1994), AB98	1.5 × 1.5	0.75	1.3
St. Marys, Ohio	07/12/86	40.55, −84.39	4.5	25, 90	5	5	Schwartz and Christensen (1988), AB98	1.5 × 1.5	0.75	1.2
Perry (Painsville), Ohio	01/31/86	41.64, −81.11	4.8	21, 84	6	8	Dziewonski *et al.* (1987), AB98	2 × 2	1	1.5
Goodnow, New York	10/07/83	43.94, −74.26	5.0	90, 60	7	16	Nábelek and Suárez (1989), AB98	2 × 2	1	1.2
Saguenay, Québec	11/25/88	48.12, −71.18	5.8	333, 51	26	18	Haddon (1992), AB98	14 × 2	2	2.2
Cornwall-Massena†, Ontario-New York	09/05/44	45.00, −74.70	5.8	0, 50	10	4	Ebel *et al.* (1986), AB98	8 × 8	2	0.5
Timiskaming†, Québec	11/01/35	46.90, −79.10	6.2	150, 50	10	6	Ebel *et al.* (1986), AB98	12 × 12	3	0.4
Nahanni, Northwest Territories	12/23/85	62.26, −124.21	6.8	175, 25	6	3	Wetmiller *et al.* (1988), AB98	25 × 15	5	1.1
Grand Banks†, Laurentian Channel	11/18/29	45.17, −57.08	7.3	122, 74	1	2	Bent (1995), AB98	80 × 16	8	0.7

*First reference gives fault parameters; second reference decribes ground-motion data.
†Historic earthquake with poorer data quality.
‡Atkinson and Boore (1998).

total moment (as described by Joyner and Boore, 1986). This summation process is approximated by the functional form used by Atkinson (1993a), Atkinson and Boore (1995, 1998), and Atkinson and Silva (1997) to match the empirically derived source spectral shape; their functional form represents the addition of Brune point sources. It is important to recognize that this spectral shape persists at all distances. Thus finite-fault effects, even from a moderate event, are not limited to near-fault distances only (Atkinson, 1993a; Atkinson and Boore, 1998).

Figure 3 explains why finite-fault simulations are more successful than a single-corner-frequency point source in reproducing the broad spectrum of recorded ground motions. There is little doubt that the radiation from large faults is formed by the consecutive ruptures of their smaller parts, whose corner frequencies are higher than those derived from full fault dimensions. This reality is neglected by the point-source approximation, while even a simple discretization appears to capture the salient effects.

The parameters of the finite-fault simulation method include the fault geometry, generic regional properties describing path effect, the subfault size, and the radiation-strength factor (which is related to maximum slip velocity). In the individual simulations of the eight digitally recorded ENA earthquakes, we explore the role of free parameters that are not constrained by crustal properties or fault geometry. The two free parameters of the model, provided that fault dimensions and orientation are fixed, are the radiation-strength factor, which controls the high-frequency spectral level, and the subfault size, which controls spectral shape. All model parameters are subsequently described.

Model Parameters

Generic ENA Model Parameters. The generic parameters that are fixed for all simulations are listed in Table 3. The attenuation and path effects are given by the ENA-specific Q, geometric spreading, and distance-dependent duration operators, as well as the kappa model, all of which are taken from Atkinson and Boore (1995). These parameters were determined by empirical analysis of regional seismographic data (Atkinson and Mereu, 1992; Atkinson and Boore, 1995; Atkinson, 1996). Exceptions to the generic kappa value are made for the Nahanni and Saguenay mainshocks. The Nahanni simulations use $\kappa = 0.010$ sec. This finding reflects the trend for kappa to increase from the ENA region to the west (Atkinson, 1996). The value of $\kappa = 0.006$ is found for the Saguenay mainshock by direct fitting of the high-frequency end of its Fourier acceleration spectra, up to the frequency of 50 Hz. Kappa values for the Saguenay strong-motion data tend to be higher than those for ENA rock sites in general, due to the location of most of the Saguenay recordings within the highly fractured Charlevoix meteor-impact structure.

Fault Geometry. For most events, there is no information on the specific rupture geometry, other than the strike and dip of the fault plane. In this case, we assume simple square faults rupturing from the center (see Table 1). There are three exceptions:

- For the Saguenay mainshock, an elongated geometry is suggested by the observed directivity (Haddon, 1992; Beresnev and Atkinson, 1997). The dimensions and rupture-initiation point for this event are as in our previous study (see later).

Table 2
Recording Stations

Station Name	Latitude (deg)	Longitude (deg)	Location
Eastern Canada Telemetered Network and Canadian National Seismographic Network (Digital Seismograms)			
A11	47.24	−70.20	St-Roch-des-Aulnaies, Québec
A16	47.47	−70.01	Rivière-Ouelle, Québec
A21	47.70	−69.69	St-André, Québec
A54	47.46	−70.41	Misère, Québec
A61	47.69	−70.09	Sainte-Mathilde, Québec
A64	47.83	−69.89	Saint-Siméon, Québec
CKO	45.99	−77.45	Chalk River, Ontario
CNQ	49.30	−68.07	Cote-Nord, Québec
CRLO	46.04	−77.38	Chalk River, Ontario
DAQ	47.96	−71.24	Lac Daran, Québec
DPQ	46.68	−72.78	St-Jean-des-Piles, Québec
DRLN	49.26	−57.50	Deer Lake, Newfoundland
EBN	47.54	−68.24	Edmundston, New Brunswick
EEO	46.64	−79.07	Eldee, Ontario
GAC	45.70	−75.48	Glen Almond, Québec
GGN	45.12	−66.82	St. George, New Brunswick
GNT	46.36	−72.37	Gentilly, Québec
GRQ	46.61	−75.86	Grand-Remous, Québec
GSQ	48.91	−67.11	Grosses-Roches, Québec
HTQ	49.19	−68.39	Hauterive, Québec
ICQ	49.52	−67.27	Islet-Caribou, Québec
JAQ	53.80	−75.72	LaGrande, Québec
KLN	46.84	−66.37	Kendrick Lake, New Brunswick
LG4Q	53.63	−74.10	LaGrande4, Québec
LMN	45.85	−64.81	Caledonia Mountain, New Brunswick
LPQ	47.34	−70.01	La Pocatière, Québec
MNQ	50.53	−68.77	Manicouagan, Québec
MNT	45.50	−73.62	Montréal, Québec
OTT	45.39	−75.72	Ottawa, Ontario
SADO	44.77	−79.14	Sadowa, Ontario
SBQ	45.38	−71.93	Sherbrooke, Québec
SCHQ	54.83	−66.83	Schefferville, Québec
SMQ	50.22	−66.70	Ste-Marguerite, Québec
SUO	46.40	−81.01	Sudbury, Ontario
TBO	48.65	−89.41	Thunder Bay, Ontario
TRQ	46.22	−74.56	Mont-Tremblant, Québec
ULM	50.25	−95.88	Lac du Bonnet, Manitoba
VDQ	48.23	−77.97	Val D'Or, Québec
WBO	45.00	−75.28	Williamsburg, Ontario
Strong-Motion Stations (Saguenay, Nahanni, and Perry Events)			
01	47.13	−70.83	St-Ferréol, Québec
02	46.78	−71.28	Québec, Québec
05	48.14	−69.72	Tadoussac, Québec
08	47.66	−70.15	La Malbaie, Québec
09	47.53	−69.81	St-Pascal, Québec
10	47.48	−70.00	Rivière-Ouelle, Québec
16	48.49	−71.01	Chicoutimi-Nord, Québec
17	48.33	−71.99	St-André-du-Lac-St-Jean, Québec
20	47.55	−70.33	Les Éboulements, Québec
01 (NAHANNI)	62.20	−124.37	Temporary epicentral deployment
02 (NAHANNI)	62.23	−124.17	Temporary epicentral deployment
03 (NAHANNI)	62.13	−123.83	Temporary epicentral deployment
PERRY	41.45	−81.11	Perry Nuclear Power Plant
Historic Observation Stations			
AAM	42.30	−83.66	Ann Arbor, Michigan
BUF	42.93	−78.85	Buffalo, New York
CHI	41.90	−87.63	Chicago, Illinois
CIN	39.09	−84.27	Cincinnati, Ohio
CSC	34.00	−81.03	Columbia, South Carolina
FOR	40.51	−73.53	Fordham, New York
GEO	38.90	−77.07	Georgetown, District Columbia
PHI	39.57	−75.09	Philadelphia, Pennsylvania
WES	42.38	−71.32	Weston, Massachusetts

- For the Nahanni event, the adopted dimensions and hypocenter location are as suggested by Weichert *et al.* (1986) and Wetmiller *et al.* (1988), based on a detailed analysis of the aftershock distribution and strong-motion directivity.
- For the Grand Banks event, we assign a rectangular fault plane and assume unilateral rupture propagation, following the work of Bent (1995, Fig. 10). However, the synthetics for this event are not sensitive to the details of assumed fault-plane geometry, because its only two recordings were made at distances of more than 1400 km, for which the distance dependence of duration is the dominant duration effect.

Subfault Size. In developing the initial simulation procedure, we constrained the subfault size (Δl) in a narrow range of values to ensure uniqueness of results (Beresnev and Atkinson, 1998a). In view of the considerations discussed in the previous section, the subfault size might alternatively be considered an essential modeling parameter, controlling the shape of the spectrum at intermediate frequencies. Modeling of ENA data, as we show later, indicates that this approach makes it possible to accurately reproduce the observed spectra in a broad frequency range, from ~0.1 to 50 Hz, over a broad range of magnitudes.

In the simulations of the eight digitally recorded ENA earthquakes, we adjusted the subfault size by trial and error to obtain the best fit to the observed spectral shape (Table 1). Figure 4 plots the best-fitting values of Δl (triangles) as a function of moment magnitude. Note that the data points corresponding to $M = 4.2$ and 4.5 actually represent four earthquakes, as seen from Table 1. The values of Δl derived from our simulations of the M 8.1 1985 Michoacan, Mexico (Beresnev and Atkinson, 1997, 1998a), and the M 6.7 1994 Northridge, California (Beresnev and Atkinson, 1998b), events are also plotted. It is apparent from Figure 4 that there is a clear trend for the best-fitting subfault size to increase linearly with the magnitude of the simulated event. Figure 4 suggests that each event with the magnitude in the range from 4 to 8 has a characteristic subevent size that allows an accurate simulation of the observed spectrum at intermediate frequencies. The encouraging feature of this trend is that it establishes a simple rule for prescribing Δl for any particular magnitude:

$$\log \Delta l = -2 + 0.4\, M \qquad (1)$$

(all logs are base 10). The simulations do not require a large number of subfaults: the ratio $L/\Delta l$, where L is the linear

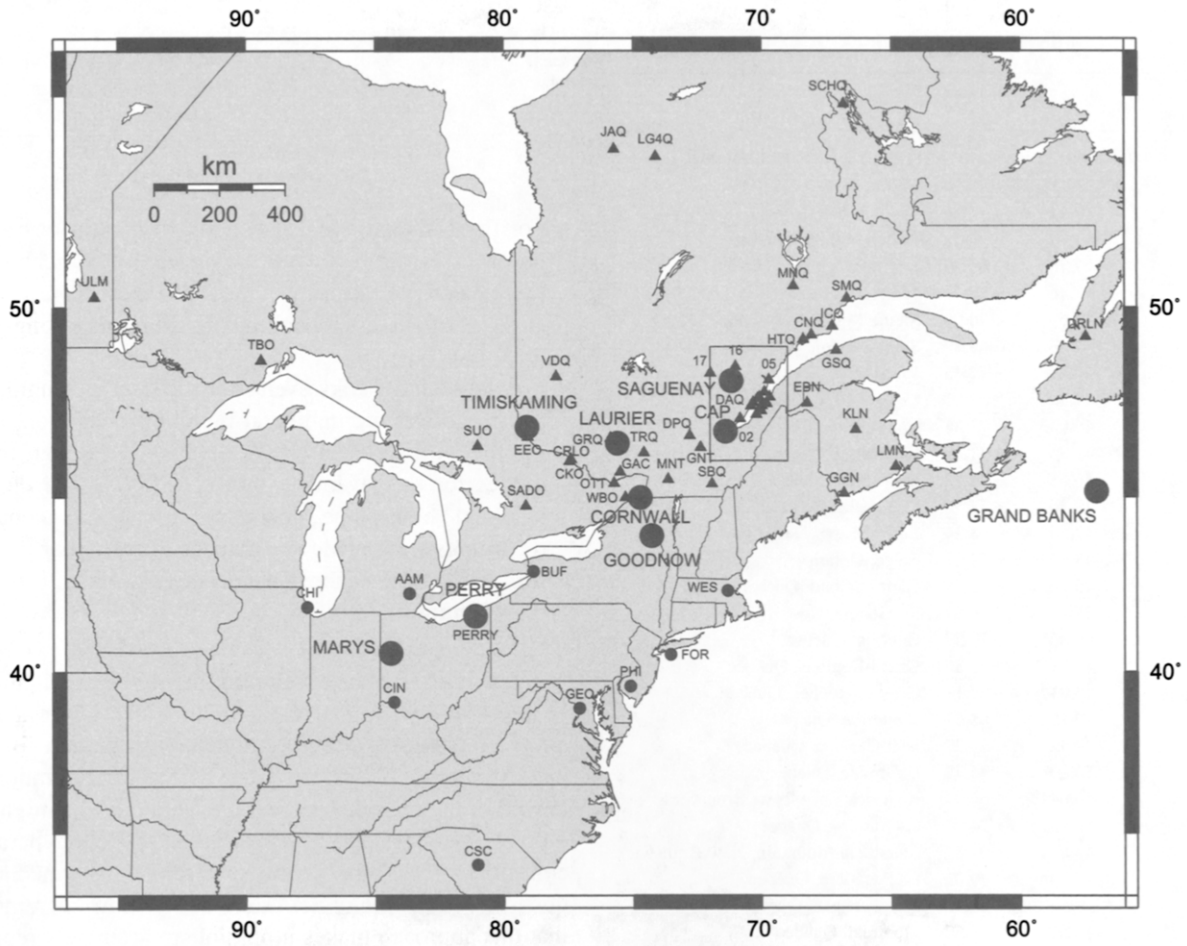

Figure 1. Epicenters of significant ENA earthquakes (large filled circles), digital seismographic and strong-motion stations (filled triangles), and stations providing historic seismograms (small filled circles). The 1985 Nahanni event lies approximately 2500 km to the northwest and is not shown. The blowup view of the area outlined by a rectangle is shown in Figure 2. The list of stations used in the analyses is provided in Table 2.

dimension of the fault, increases from 2 for the $M \sim 4$ to 5 earthquakes to 10 for the Michoacan event ($M = 8.1$).

Radiation-Strength Factor. If we accept the hypothesis that the subfault size is unambiguously defined by the magnitude of the simulated event, as suggested by Figure 4 (equation 1), then it can no longer be considered a free parameter of the model. In this situation, as seen from Tables 1 and 3, the radiation-strength factor (s) becomes the only adjustable parameter of the finite-fault simulations.

The parameter s was introduced by Beresnev and Atkinson (1998a) to measure the strength of high-frequency radiation from faults: it controls the level of the acceleration spectra above the corner frequency of the subfaults. The slip for the dislocation that radiates the ω^2 spectrum is described by the exponential function

$$u(t) = u(\infty)[1 - (1 + \omega_0 t)e^{-\omega_0 t}], \qquad (2)$$

where u and $u(\infty)$ are the dislocation displacement and its asymptotic value, $\omega_0 \equiv 2\pi f_0$, and f_0 is the corner frequency of the spectrum (Brune, 1970, equation 13; Tumarkin and Archuleta, 1994, equation 1.2; Beresnev and Atkinson, 1997, equation 6). From equation (2), the corner frequency characterizes the dislocation growth rate, or the speed at which the fault approaches its static displacement. Because it formally takes an infinite time for the function (2) to rise to the level of $u(\infty)$, a convention is needed on how to define its rise time. A common convention is to define rise time as $T_{1/2}$, or the time when the level of $u(\infty)/2$ is reached. If we define $\omega_0 T_{1/2} \equiv z$ in (2), it follows from (2) that $z = 1.68$. Finally, we postulate that the local rise time equals the time it takes for the rupture to propagate from one end of the fault to the other. This gives

$$\omega_0 = yz \frac{\beta}{L}, \qquad (3)$$

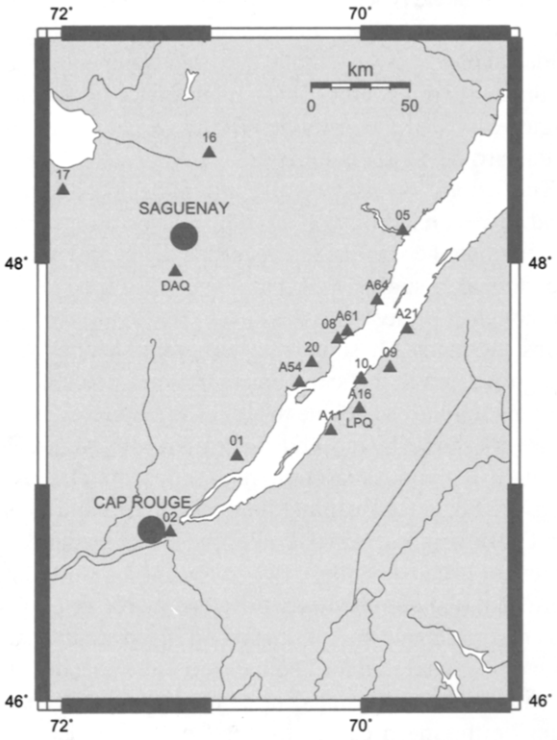

Figure 2. Seismographic and strong-motion stations providing data for the Charlevoix Seismic Zone (blowup view of the area outlined by a rectangle in Fig. 1).

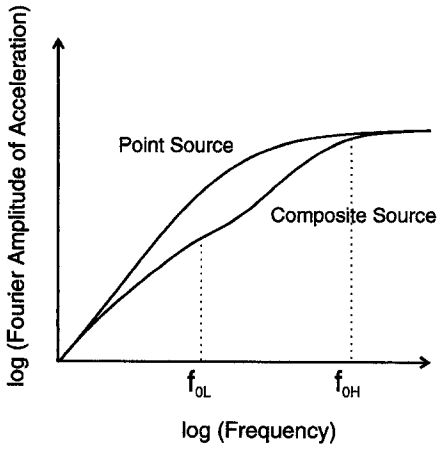

Figure 3. Comparison of the spectrum resulting from the summation of subevent point sources over a finite fault plane (lower line), with a single ω^2 spectrum, having the same moment magnitude and high-frequency spectral level (upper line). f_{0H} is the subfault corner frequency. f_{0L} is the second (low-frequency) corner produced by the summation procedure, under the conservation-of-moment constraint.

Table 3
Generic Modeling Parameters for Eastern North America

Parameter	Parameter Value
$Q(f)$	$670f^{0.33}$
Geometric spreading	$1/R$ ($R \leqq 70$ km)
	$1/R^0$ ($70 < R \leqq 130$ km)
	$1/R^{0.5}$ ($R > 130$ km)
Distance-dependent duration term (sec)	0 ($R \leqq 10$ km)
	$0.16\,R$ ($10 < R \leqq 70$ km)
	$-0.03\,R$ ($70 < R \leqq 130$ km)
	$0.04\,R$ ($R > 130$ km)
Crustal amplification	Boore–Joyner (1997) ENA
Kappa (parameter of low-pass filter) (sec)	0.002
Stress parameter (bars)	50
Windowing function	Saragoni–Hart
Crustal shear-wave velocity (km/sec)	3.6
Rupture velocity	0.8 × (shear-wave velocity)
Crustal density (g/cm^3)	2.8
Fault-slip distribution	uniform
Stochastic trials to generate response spectrum	3

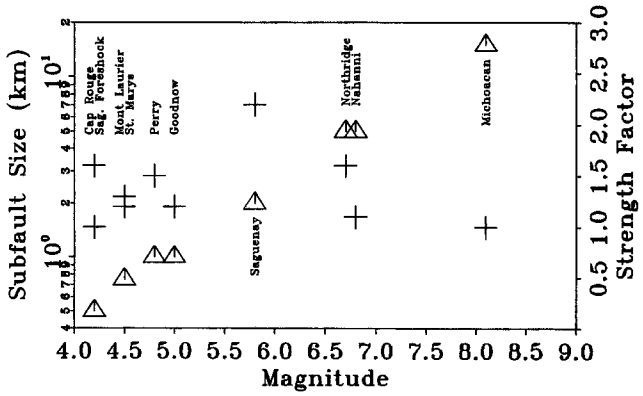

Figure 4. Subfault size (triangles, left axis) and radiation-strength factor (crosses, right axis) that best fit the observed spectra, as a function of target moment magnitude. The values suggested by our previous modeling of the 1985 Michoacan, Mexico, and the 1994 Northridge, California, events are also shown. Historic ENA events have insufficient high-frequency bandwidth to constrain these parameters and are not plotted.

where β is the shear-wave velocity, and y is the ratio of the rupture-propagation velocity to β, set to a value of 0.8 (modified from Beresnev and Atkinson, 1997, equation 14).

From equation (2), $v_m = \omega_0 u(\infty)/e$, where v_m is the maximum rate (time derivative) of dislocation displacement and e is the base of the natural logarithm. Using the definition of the stress parameter $\Delta\sigma \equiv \mu u(\infty)/L$, where μ is the shear modulus, equation (3) can be rewritten as

$$v_m = \frac{yz}{e}\frac{\Delta\sigma}{\rho\beta}, \tag{4}$$

where ρ is the density (modified from Beresnev and Atkin-

son, 1998a, equation 3). We thus obtain the quantity z in (3) and (4) as a scaling factor that is related to the maximum slip velocity on the fault. The amplitude level of the acceleration spectrum at high frequencies, radiated from the finite fault, is proportional to z^2 (Beresnev and Atkinson, 1998a, equation 6), or the slip velocity squared. The slip velocity corresponding to $z = 1.68$ can be considered a standard value, in that it reflects the most common convention used to define rise time. Deviations below or above this value may be interpreted as describing slower or faster fault slips, respectively, relative to this standard condition. The value of z for each particular earthquake can be obtained from fitting its high-frequency spectral level. Its ratio to the value of 1.68 is referred to as the radiation-strength factor; this factor reflects the actual slip velocity, relative to the standard velocity. The standard event thus has $s = 1$.

There is a degree of arbitrariness in defining the standard value of z. However, it appears to have some empirical basis. By fitting the recorded near-fault acceleration spectra, we determined the strength-factors for the well-documented 1985 Michoacan, Mexico, and 1994 Northridge, California, earthquakes. The corresponding values of maximum slip velocities, as determined from (4), were in good agreement with those obtained from a literature survey of detailed fault rupture models for these events (Beresnev and Atkinson, 1998a, 1998b). The best-fitting s values for all simulated ENA events are listed in Table 1 and plotted as crosses in Figure 4.

Comparison of Simulation Results to Data

Simulation of Individual Events

To quantify the goodness of fit of ground-motion synthetics to observed data, we use the criterion of model bias. Specifically, we show the difference between the logarithms (base 10) of the observed and the simulated spectrum, averaged over all recording sites (Abrahamson *et al.,* 1990; Schneider *et al.,* 1993; Atkinson and Boore, 1998). This definition emphasizes the spectral content of ground motions, which is particularly relevant for engineering applications. Figure 5 presents model bias and its standard deviation for the 11 modeled ENA events. Simulations of all individual spectra are presented in the Appendix (Figures A1 to A11). The number of stations for each event, from which the mean bias and the standard deviation were calculated, is indicated in Table 1.

The best-fitting subfault size and the strength factor for each individual event are chosen as to minimize model bias over the entire frequency band. The subfault size controls the spectral fall-off below the corner frequency of the subsources and thus affects the depth of the intermediate-frequency sag. The strength factor controls the spectral level above the subfault corner frequency. The bias can be minimized by jointly varying these two parameters. The subfault sizes determined in this way are those plotted in Figure 4.

The number, type, and quality of recordings vary from event to event, resulting in variable frequency range and confidence bands. For example, the 1985 Nahanni event had only three recording sites. This explains why the mean bias in Figure 5 is poorly constrained for this event, even though the standard deviation is fairly small.

The historic events generally suffer from poor data quality and suspect reliability of individual observations. For example, among the stations that recorded the 1935 Timiskaming earthquake, station BUF has the lowest spectral level, even though it is closest to the epicenter (Figure A9). Also, stations PHI and CHI show very different spectral values, although located at the same epicentral distance. Such variations are unlikely to be due to local site responses, because they are not shown by the well-recorded recent events. However, without obvious reasons to reject any particular historic record, we opted for retaining them all. An exception is the 1925 Charlevoix earthquake. We chose not to model the 1925 event because its only two recordings were mutually inconsistent (e.g., implied very different source amplitudes); in this circumstance, we felt that any derived source parameters would be unreliable. The inclusion of all records from each modeled event resulted in comparatively large uncertainties on the mean curves for the Cornwall-Massena and Timiskaming events (Fig. 5). For the 1929 Grand Banks earthquake, there are only two useable records; therefore, we plotted the individual station biases (FOR and AAM), instead of showing the mean. The historic data are limited to low frequencies, because the instruments could not recover amplitudes for frequencies above 1 Hz (Atkinson and Chen, 1997). This frequency range does not allow the data to constrain either the subfault size or the high-frequency radiation-strength factor; therefore, these events are not plotted in Figure 4. On the contrary, we used equation (1), as derived from Figure 4, to determine the subfault sizes for these events ($\Delta l = 2, 3$, and 8 km for the Cornwall-Massena, Timiskaming, and Great Banks earthquakes, respectively) (Table 1). This provided a check on whether model constraints derived from the analysis of recent events are consistent with historic data. The radiation-strength factors listed for the historic events in Table 1 are those that provide the best fit to the data, but we caution that these values have no real meaning due to the lack of high-frequency amplitude data.

Most of the modern events were recorded on the Eastern Canada Telemetered Network (ECTN) during the 1980s. The ECTN is a short-period network, with useable frequency range from about 1 to 10 Hz. By the time of the occurrence of the 1997 Cap Rouge earthquake, many of the ECTN stations had been replaced with the new broadband instruments of the Canadian National Seismographic Network (CNSN), which have a broader frequency band. The useable frequency band in the Cap Rouge simulations is thus from 0.1 to 20 Hz (Fig. A1).

Because the Saguenay and the Nahanni earthquakes provided near-fault acceleration data over a broad frequency

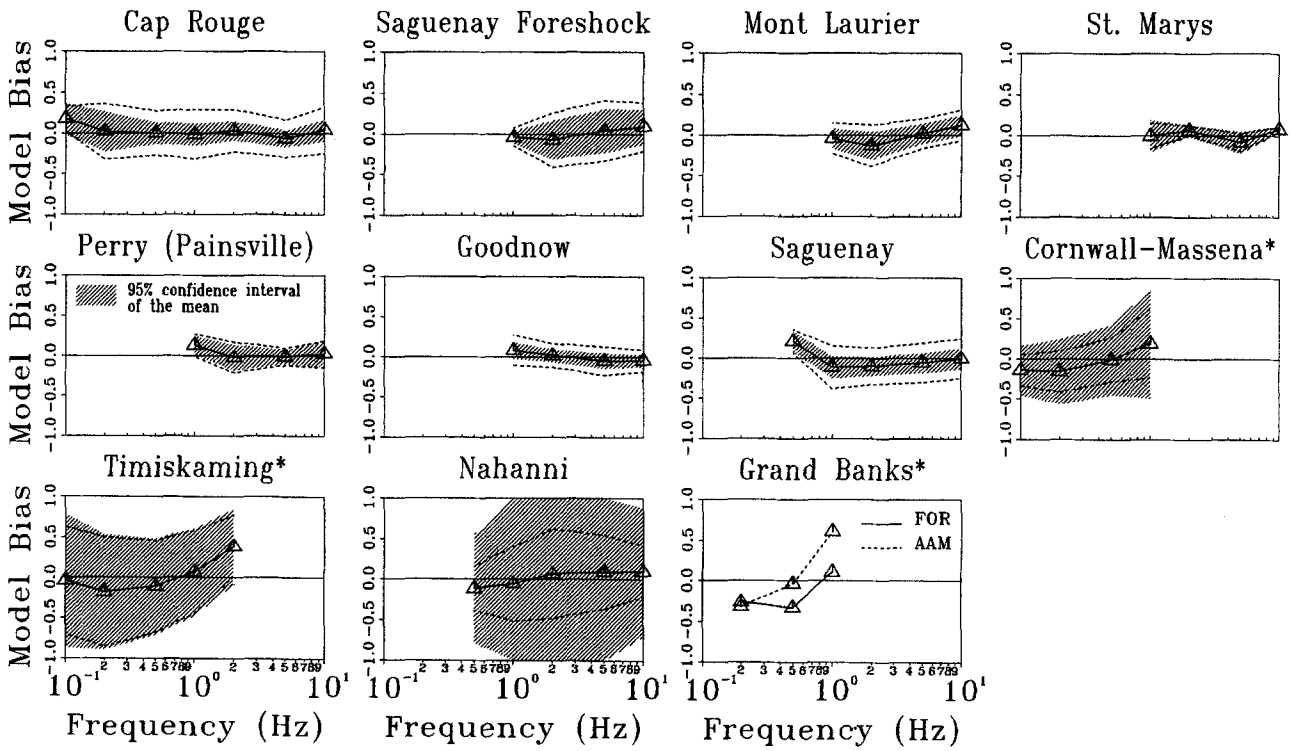

Figure 5. Model bias, calculated as the difference between the logarithms of the observed and the simulated spectrum, averaged over all recordings for the event. The 5% damped response spectra were used. Bias is calculated at frequencies of 0.1, 0.2, 0.5, 1, 2, 5, and 10 Hz (triangles). The observed response spectral values are taken from the ENA spectral database (Atkinson and Boore, 1998). The hatched band shows 95% confidence limits of the mean calculated from the *t* distribution, and dashed lines show ± one standard deviation. Historical events (having less-reliable data) are marked with the asterisks.

range, we found it useful to conduct a separate detailed modeling of their strong-motion records. The same model parameters as for the regional stations were used. Figure 6 shows a comparison between the observed and simulated Fourier spectra and acceleration time histories at nine strong-motion sites of the Saguenay mainshock. This is a revisit of our previous modeling of these data (Beresnev and Atkinson, 1997), now performed in the framework of a uniform procedure adopted for all ENA events. The usable frequency range is 0.5 to 50 Hz, and all spectra are sampled at 0.05 Hz. The stations are arranged clockwise from the northwest direction. According to the observed directivity, the rupture propagated unilaterally toward the southeast along the northwest–southeast-striking fault. The directivity effects caused an increase in ground-motion duration toward the northwest (stations 17 and 16), opposite to the rupture-propagation direction. This can be clearly seen in both the observed and simulated traces. Figure 7 shows the mean model bias and its standard deviation for this event, obtained from Fourier spectra.

Figures 8 and 9 present individual-station simulations and model bias for the Nahanni event. The wider confidence limits of the mean reflect the fact that the records are available at only three stations, and thus the mean is poorly constrained, despite the reasonably low standard deviation. The records at station 1 are puzzling, with the most energetic pulse arriving late in the signal, at approximately 8 sec (Fig. 8). This portion of the record has extraordinarily high peak accelerations of approximately 1.3 and 0.98 *g*. The strongest trace excursions on the original paper records overlapped badly and were clipped; they were reconstructed later rather intuitively (Weichert *et al.*, 1986). This causes ambiguity in the overall spectral level at station 1. The nature of the peaks is also left unexplained. While the smooth rupture-propagation model satisfactorily explains the shape and the peak accelerations of the recorded traces at stations 2 and 3, it underpredicts peak acceleration values at station 1 by more than a factor of 2 and does not explain the post-8-sec arrivals (Fig. 8). This clearly increases the model uncertainty shown in Figure 9.

Model Uncertainty

Figures 5, 7, and 9 show that, for the eight digitally recorded events, the finite-fault simulations provide an unbiased fit to the observed motions, when the subfault size is as given in equation (1), and the high-frequency radiation

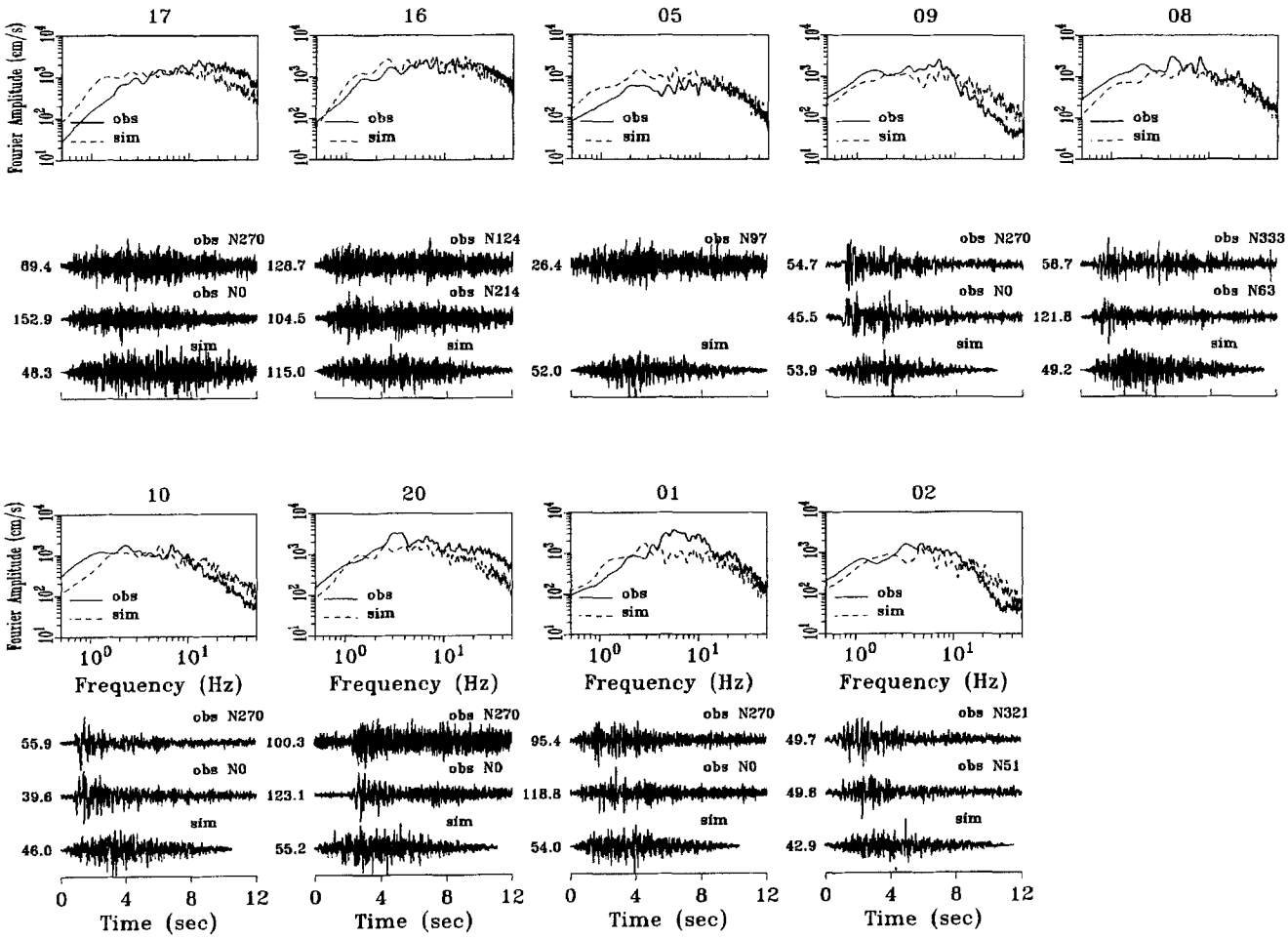

Figure 6. Comparison of recorded and simulated Fourier amplitude spectra and accelerograms at the nine strong-motion sites that recorded the Saguenay mainshock. The recorded and simulated spectra are shown by the solid and dashed lines, respectively. The station number is indicated on top of each plot. The two upper traces below the spectra are the observed horizontal accelerations, with the azimuth of the component indicated above each trace. At station 05, only one horizontal component is available. The lower trace is the simulated accelerogram. The peak ground acceleration in cm/sec^2 is shown to the left of the traces.

strength factor (s) is chosen so as to provide the best fit to high-frequency spectral level. The mean bias is within the 95% confidence limits of zero. The maximum excursion from zero is 0.2 log units, or a factor of 1.6, in all cases. Even though Δl for the historic earthquakes was not used to construct the relationship in Figure 4, Δl assumed from it provides a satisfactory average fit to the historic data as well, although with larger uncertainties (Fig. 5). These uncertainties are expected due to the poorer quality of the historic recordings.

Figures 6 and 8 show that the character of the observed acceleration time histories is reproduced well in the simulations. The simulations explain the azimuthal change in the shape and duration of ground motion resulting from rupture-propagation effects.

Figure 10 shows the overall simulation bias when averaged over all 105 records, from all 11 events. In general, a simple average over all records (i.e., equal-record weighting) may place undue weight on events with the most recordings. In this case, this problem is not severe, because the model is unbiased for each individual event, due to the adjustment of the model parameters Δl and s. The simple average over all records indicates that the model is unbiased at all frequencies ranging from 0.1 to 10 Hz. The total standard deviation of the ratio of observed to simulated spectra is about 0.25 log units (a factor of 1.8) at frequencies above 1 Hz; it increases to about 0.40 log units (a factor of 2.5) below 1 Hz. As seen from Figure 5, the low-quality data from the historic events contributed most to the bias estimated below 0.5 Hz, causing larger uncertainty. Apart from the historic records, only the 1997 Cap Rouge earthquake, recorded on broadband instruments, provided data at low frequencies. The Cap Rouge simulations (Fig. 5) suggest that model bias does not increase dramatically at low frequencies.

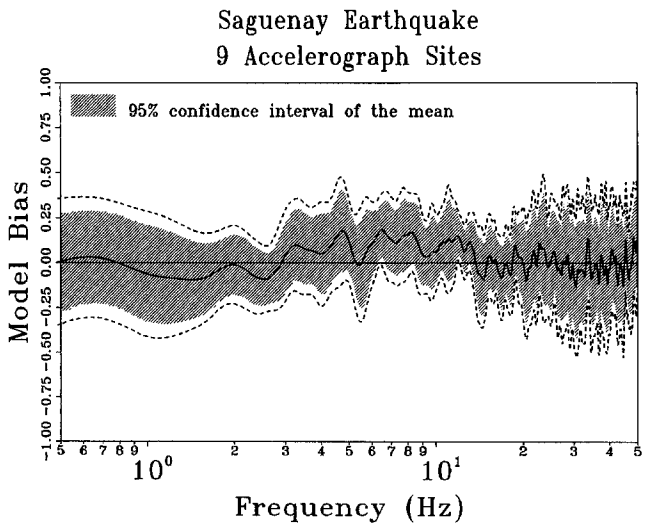

Figure 7. Model bias and its standard deviation for the Saguenay strong-motion simulations, calculated from the Fourier spectra at the nine strong-motion stations, sampled at 0.05 Hz. The observed spectrum at each station is calculated as the geometric average of the spectra of the two horizontal components, except for station 05, where only one horizontal component is available.

Discussion

The stochastic finite-fault model, which treats earthquakes as a summation of Brune point sources, distributed over a finite fault plane, provides accurate ground-motion estimates for ENA earthquakes of M 4 to 7, over the frequency range from 0.1 to 50 Hz. In this sense, the finite-fault model serves as a conceptual foundation for the empirical source model used by Atkinson and Boore (1995) in their ENA ground-motion relations. Atkinson and Boore (1998) show that a two-corner point-source spectrum, containing the same spectral sag that is predicted by the finite-fault model, also matches these data. By contrast, the single-corner-frequency Brune point-source model systematically overpredicts ground-motion amplitudes at low to intermediate frequencies, even for moderate events at large distances (Atkinson and Boore, 1998).

The key assumption in the finite-fault simulations that leads to the improved agreement between simulated and observed spectra (relative to the Brune point source) is the representation of fault radiation as a sum of contributions from smaller subfaults (each of which has an ω^2 point-source spectrum). The subfault corner frequency is higher than that derived from the full fault dimension. It follows that the subfault size in kinematic source models should be considered an essential model parameter, which cannot be arbitrarily chosen. However, we found that Δl, determined by fitting the recorded data, exhibits a clear linear dependence on the magnitude of the target event (Fig. 4). This suggests that there are strong similarities in the rupture processes of the events over a wide magnitude range. Even the smallest events, with magnitudes as low as 4.2, need to be treated as composite ruptures. On the other hand, none of the events, not even the largest ones, require fine discretization to match the observed spectra. The ratio of $L/\Delta l$, where L is the characteristic fault dimension (e.g., fault length), increases from 2 to 10 over a magnitude difference of four units.

Figure 4 suggests that the size of the subevent for an earthquake of any particular magnitude may be characteristic, at least in the context of this model. If the subfault size can be unambiguously associated with the magnitude of the simulated event, Δl is no longer a free model parameter, and the model becomes well constrained. The only remaining free parameter of finite-fault simulations is the radiation-strength factor, which may be reflective of the natural variability of slip velocities on rupturing faults.

The strength factors (or slip velocities) do not appear to vary significantly among the different earthquakes, at least in the cases studied, suggesting another important similarity in the rupture processes. From our simulation results in this and previous studies, the parameter s generally falls in the range from 1.0 to 1.6. This excludes the historic events, which do not have adequate high-frequency bandwidth to constrain s. The sole exception among the digitally recorded earthquakes is the Saguenay mainshock, with $s = 2.2$. We infer that the slip on the Saguenay fault may have been anomalously fast, perhaps due to its deep focal depth. The strength factor is also apparently independent of moment magnitude (Fig. 4).

Our adopted ENA path-effect model may be biased at distances exceeding approximately 1000 km. Our model for Q, geometric spreading, and distance-dependent duration (Table 3) was developed by Atkinson and Mereu (1992) and Atkinson and Boore (1995), based on data recorded at distances less than 1000 km. The 1997 Cap Rouge earthquake provided high-quality seismographic data covering distances from approximately 100 to 1800 km. As seen from Figure A1, the adopted path-effect model appears to systematically underpredict data for stations beyond 1000 km, at least for this event. We also note that the largest uncertainties in our modeling of the historic earthquakes are associated with the Grand Banks event, whose observed spectral shape is not well matched by synthetics (Figs. 5 and A11). One obvious reason for this uncertainty, mentioned earlier, is that this event is represented by only two stations, both of which are of suspect reliability. However, these sites are also at distances of approximately 1500 and 2200 km from the source, where the path-effect model may break down.

In summary, with the subfault size determined by the magnitude from the relationship in Figure 4 (equation 1), and considering the best-fitting s factor, the mean ground-motion prediction bias is indistinguishable from zero for all eight digitally recorded ENA earthquakes of $M > 4$. For all frequencies between 0.1 and 50 Hz, the value of the mean bias for any individual event does not exceed 0.2 log units (a factor of 1.6). When averaged over all records, the simu-

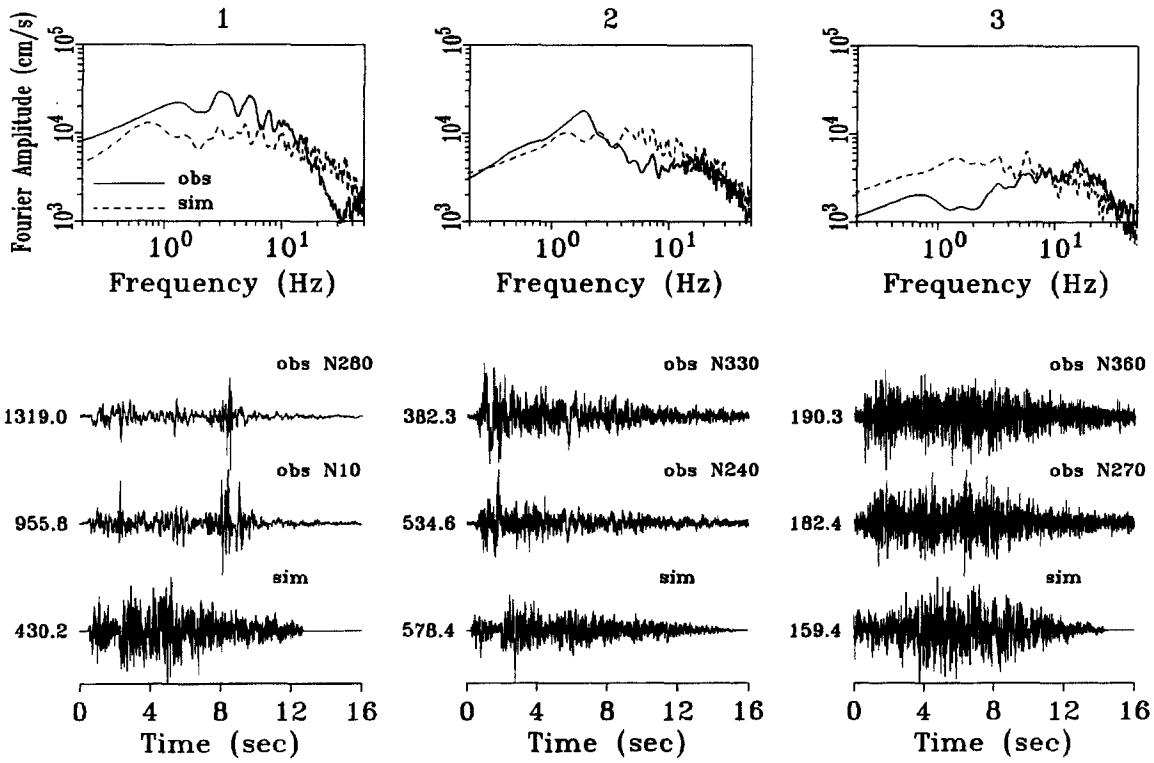

Figure 8. Comparison of recorded and simulated Fourier amplitude spectra and accelerograms at the three strong-motion sites that recorded the Nahanni mainshock. The recorded and simulated spectra are shown by the solid and dashed lines, respectively. The station number is indicated on top of each plot. The two upper traces below the spectra are the observed horizontal accelerations, with the azimuth of the component indicated above each trace. The lower trace is the simulated accelerogram. The peak ground acceleration in cm/sec^2 is shown to the left of the traces.

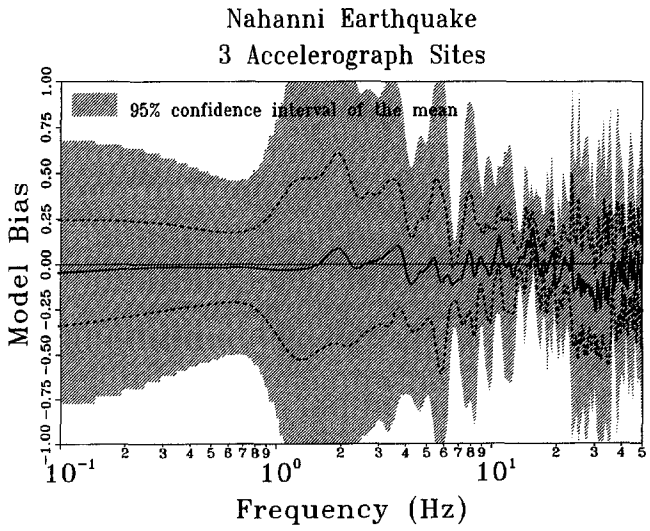

Figure 9. Model bias and its standard deviation for the Nahanni strong-motion simulations, calculated from the Fourier spectra at the three strong-motion stations, sampled at 0.05 Hz. The observed spectrum at each station is calculated as the geometric average of the spectra of the two horizontal components.

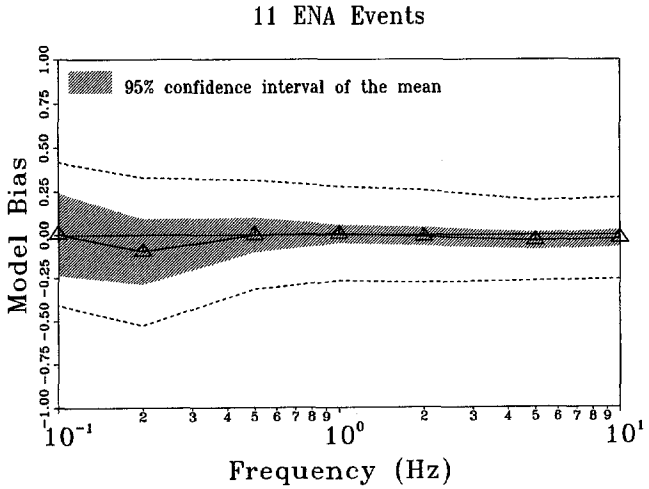

Figure 10. Model bias averaged over all earthquakes and stations (105 records).

lation is unbiased at all frequencies. The standard deviation of the ratio of observed to simulated spectra corresponds to about a factor of 2 uncertainty in ground-motion prediction, in the frequency range from 0.1 to 50 Hz.

It is useful to compare our finite-fault simulation results with the point-source results of Atkinson and Boore (1995, 1998), in order to understand the similarities and differences between these approaches. Both approaches recognize, either explicitly or implicitly, that finite-fault effects cause the radiated spectra of moderate-to-large earthquakes to differ significantly from a single-corner-frequency spectrum. Specifically, a sag appears in the spectrum at intermediate frequencies, relative to the Brune spectrum, and this sag becomes more pronounced as magnitude increases. In the work of Atkinson and Boore (1995, 1998), this is modeled by using an empirical two-corner source model (Atkinson, 1993a) to capture the salient effects on spectral amplitudes. In other words, finite-fault effects are implicitly accommodated by the use of an equivalent point-source spectrum. In the approach of this article, the finite-fault effects are treated explicitly through the representation of the extended fault plane by Brune point-source subevents. The resulting average spectrum closely resembles the equivalent point-source spectrum of Atkinson and Boore in shape and amplitude levels. Because the subfault size in our finite-fault model controls the sag at intermediate frequencies, its prescription through equation (1) is analogous to the adoption of the two-corner source model used by Atkinson and Boore (1998).

Both the finite-fault and two-corner point-source models provide an unbiased fit to the observations on average. At first glance, the finite-fault modeling of this article might appear to provide a better fit to the data. In this model, each of the digitally recorded ENA events has a bias that is indistinguishable from zero. For the two-corner point-source model, by comparison, there are significant residuals for some of the events, with an average over all events being required to achieve zero bias (Atkinson and Boore, 1998). However, Atkinson and Boore used a prescriptive two-corner spectrum dependent only on magnitude and distance to model all events. Therefore, their average event residuals measure the uncertainty in prediction of ground motions from future earthquakes, for which just magnitude and distance are known. In this article, by contrast, we used the best-fit value of the radiation strength factor, s, to model each event individually. (Because s controls the high-frequency level of the earthquake, the use of the best-fitting s for each event is equivalent to using the best-fit stress drop for each event.) We can predict the average value of s for future events but not the specific value for each event. Thus, the uncertainty in prediction of ground-motion amplitudes for future earthquakes, as a function of just magnitude and distance, is greater than that indicated by the model bias of our finite-fault modeling. Consequently, we cannot conclude that the finite-fault model provides a more accurate prediction of average ground motions for a future earthquake than does the equivalent two-corner point source. Overall, if the fault orientation is known, then the finite-fault model will be more accurate for predictions at individual sites, since it incorporates average directivity effects and provides the correct ground-motion duration based on fault rupture time. If the fault orientation is unknown, then the finite-fault and two-corner point-source models are approximately equivalent.

Acknowledgments

Most of the ground-motion data used in this article were recorded by seismographic or strong-motion stations operated by the Geological Survey of Canada and retrieved with the invaluable technical assistance of their staff, particularly Bill Shannon and Allison Bent. We thank J. Adams for providing us with focal mechanism information for some of the events. Figures 1 and 2 were produced with the Generic Mapping Tools (GMT) (Wessel and Smith, 1995). Strong-motion accelerograms for the Nahanni and Saguenay earthquakes were downloaded from the National Center for Earthquake Engineering Research (NCEER) Strong-Motion Data Base, located at Lamont-Doherty Earth Observatory of Columbia University. We are indebted to D. Boore, M. Chapman, W. Joyner, and L. Hutchings for their thoughtful reviews of the article. This study was supported by Grant 1434-HQ-97-GR-03061 from the National Earthquake Hazards Reduction Program. The FORTRAN code FINSIM used in the simulations with copies of all input files used to generate synthetics are available to all interested parties by writing to the authors.

References

Abrahamson, N. A., P. G. Somerville, and C. A. Cornell (1990). Uncertainty in numerical strong motion predictions, in *Proc. of the Fourth U.S. National Conference on Earthquake Engineering,* Palm Springs, California, Vol. 1, 407–416.

Adams, J. (1995). The Canadian crustal stress database—a compilation to 1994. Part 1—description of the database; Part 2—listing of the database on diskette, *Geol. Surv. Canada Open-File Rept. 3122,* Ottawa, Ontario, 36 pp. plus 1 diskette.

Atkinson, G. M. (1984). Attenuation of strong ground motion in Canada from a random vibrations approach, *Bull. Seism. Soc. Am.* **74,** 2629–2653.

Atkinson, G. M. (1993a). Earthquake source spectra in eastern North America, *Bull. Seism. Soc. Am.* **83,** 1778–1798.

Atkinson, G. M. (1993b). Notes on ground motion parameters for eastern North America: duration and *H/V* ratio, *Bull. Seism. Soc. Am.* **83,** 587–596.

Atkinson, G. M. (1996). The high-frequency shape of the source spectrum for earthquakes in eastern and western Canada, *Bull. Seism. Soc. Am.* **86,** 106–112.

Atkinson, G. M. and D. M. Boore (1995). Ground-motion relations for eastern North America, *Bull. Seism. Soc. Am.* **85,** 17–30.

Atkinson, G. M. and D. M. Boore (1998). Evaluation of models for earthquake source spectra in eastern North America, *Bull. Seism. Soc. Am.* **88,** 917–934.

Atkinson, G. M. and S. Z. Chen (1997). Regional seismograms from historical earthquakes in southeastern Canada, *Seism. Res. Lett.* **68,** 797–807.

Atkinson, G. M. and R. F. Mereu (1992). The shape of ground motion attenuation curves in southeastern Canada, *Bull. Seism. Soc. Am.* **82,** 2014–2031.

Atkinson, G. M. and W. Silva (1997). An empirical study of earthquake source spectra for California earthquakes, *Bull. Seism. Soc. Am.* **87,** 97–113.

Bent, A. L. (1995). A complex double-couple source mechanism for the

M_s 7.2 1929 Grand Banks earthquake, *Bull. Seism. Soc. Am.* **85,** 1003–1020.

Beresnev, I. A. and G. M. Atkinson (1997). Modeling finite-fault radiation from the ω^n spectrum, *Bull. Seism. Soc. Am.* **87,** 67–84.

Beresnev, I. A. and G. M. Atkinson (1998a). FINSIM—a FORTRAN program for simulating stochastic acceleration time histories from finite faults, *Seism. Res. Lett.* **69,** 27–32.

Beresnev, I. A. and G. M. Atkinson (1998b). Stochastic finite-fault modeling of ground motions from the 1994 Northridge, California, earthquake. I. Validation on rock sites, *Bull. Seism. Soc. Am.* **88,** 1392–1401.

Boatwright, J. and G. L. Choy (1992). Acceleration source spectra anticipated for large earthquakes in northeastern North America, *Bull. Seism. Soc. Am.* **82,** 660–682.

Boore, D. M. (1983). Stochastic simulation of high-frequency ground motions based on seismological models of the radiated spectra, *Bull. Seism. Soc. Am.* **73,** 1865–1894.

Boore, D. M. and G. M. Atkinson (1987). Stochastic prediction of ground motion and spectral response parameters at hard-rock sites in eastern North America, *Bull. Seism. Soc. Am.* **77,** 440–467.

Boore, D. M. and G. M. Atkinson (1992). Source spectra for the 1988 Saguenay, Quebec, earthquakes, *Bull. Seism. Soc. Am.* **82,** 683–719.

Boore, D. M. and W. B. Joyner (1997). Site amplifications for generic rock sites, *Bull. Seism. Soc. Am.* **87,** 327–341.

Brune, J. N. (1970). Tectonic stress and the spectra of seismic shear waves from earthquakes, *J. Geophys. Res.* **75,** 4997–5009.

Dziewonski, A. M., G. Ekström, J. E. Franzen, and J. H. Woodhouse (1987). Centroid-moment tensor solutions for January–March 1986, *Phys. Earth Planet. Interiors* **45,** 1–10.

Ebel, J. E., P. G. Somerville, and J. D. McIver (1986). A study of the source parameters of some large earthquakes of northeastern North America, *J. Geophys. Res.* **91,** 8231–8247.

Haddon, R. A. W. (1992). Waveform modeling of strong-motion data for the Saguenay earthquake of 25 November 1988, *Bull. Seism. Soc. Am.* **82,** 720–754.

Hanks, T. C. and R. K. McGuire (1981). The character of high-frequency strong ground motion, *Bull. Seism. Soc. Am.* **71,** 2071–2095.

Joyner, W. B. and D. M. Boore (1986). On simulating large earthquakes by Green's-function addition of smaller earthquakes, in *Proc. of the Fifth Maurice Ewing Symposium on Earthquake Source Mechanics,* S. Das, J. Boatwright, and C. Scholz (Editors), American Geophysical Union, 269–274.

Lamontagne, M., H. S. Hasegawa, D. A. Forsyth, G. G. R. Buchbinder, and M. Cajka (1994). The Mont-Laurier, Québec earthquake of 19 October 1990 and its seismotectonic environment, *Bull. Seism. Soc. Am.* **84,** 1506–1522.

Nábelek, J. and G. Suárez (1989). The 1983 Goodnow earthquake in the central Adirondacks, New York: rupture of a simple, circular crack, *Bull. Seism. Soc. Am.* **79,** 1762–1777.

Nadeau, L., M. Lamontagne, R. J. Wetmiller, P. Brouillette, A. L. Bent, and P. Keating (1998). Preliminary results and tectonic setting of the Cap-Rouge (Québec) earthquake of November 5th, 1997, *Current Research,* Geological Survey of Canada, Ottawa, Ontario (in press).

Schneider, J. F., W. J. Silva, and C. Stark (1993). Ground motion model for the 1989 *M* 6.9 Loma Prieta earthquake including effects of source, path, and site, *Earthquake Spectra* **9,** 251–287.

Schwartz, S. Y. and D. H. Christensen (1988). The 12 July 1986 St. Marys, Ohio earthquake and recent seismicity in the Anna, Ohio seismogenic zone, *Seism. Res. Lett.* **59,** 57–62.

Toro, G. R., N. A. Abrahamson, and J. F. Schneider (1997). Model of strong ground motions from earthquakes in central and eastern North America: best estimates and uncertainties, *Seism. Res. Lett.* **68,** 41–57.

Tumarkin, A. G. and R. J. Archuleta (1994). Empirical ground motion prediction, *Ann. Geofis.* **37,** 1691–1720.

Weichert, D. H., R. J. Wetmiller, and P. Munro (1986). Vertical earthquake acceleration exceeding 2 *g*? The case of the missing peak, *Bull. Seism. Soc. Am.* **76,** 1473–1478.

Wessel, P. and W. H. F. Smith (1995). New version of the Generic Mapping Tools released, *EOS* **76,** 329.

Wetmiller, R. J., R. B. Horner, H. S. Hasegawa, R. G. North, M. Lamontagne, D. H. Weichert, and S. G. Evans (1988). An analysis of the 1985 Nahanni earthquakes, *Bull. Seism. Soc. Am.* **78,** 590–616.

Appendix

Figures A1 to A11 present simulations of all individual spectra.

Department of Geological & Atmospheric Sciences
Iowa State University
253 Science I
Ames, Iowa 50011-3212
E-mail: beresnev@iastate.edu
(I. A. B.)

Department of Earth Sciences
Carleton University
1125 Colonel By Drive
Ottawa, Ontario K1S 5B6, Canada
E-mail: gma@ccs.carleton.ca
(G. M. A.)

Manuscript received 20 July 1998.

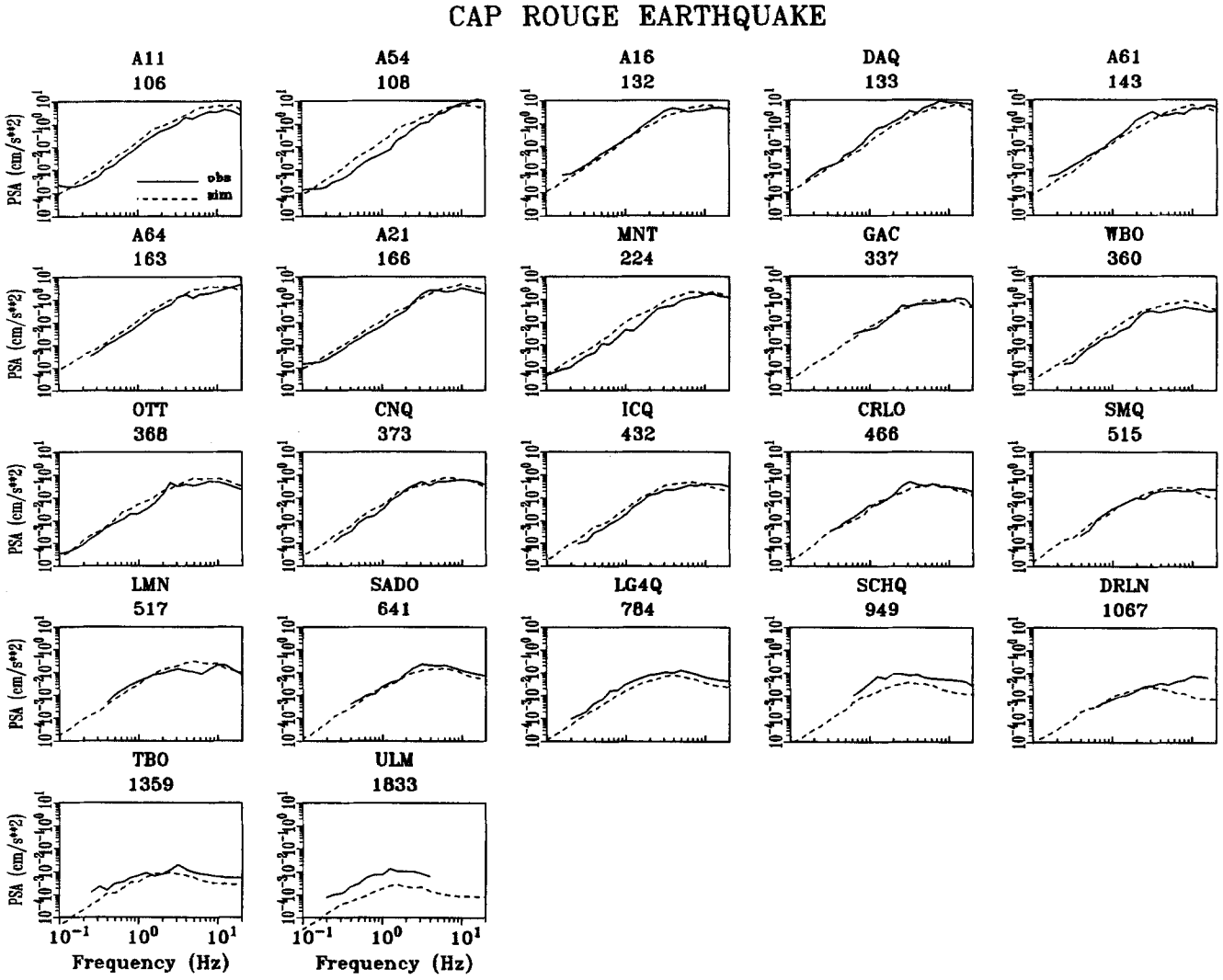

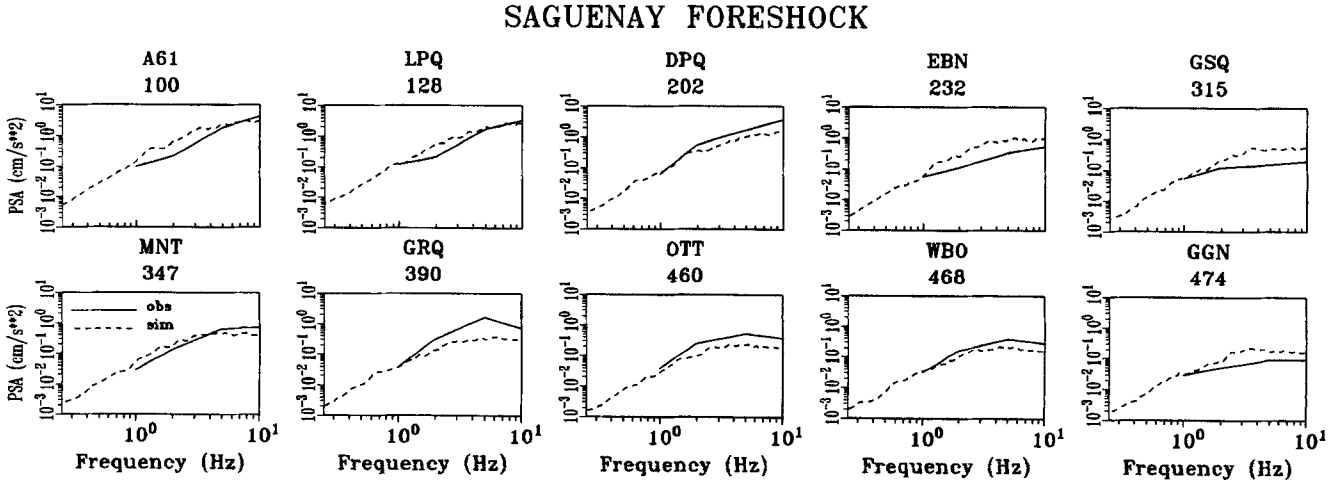

Figure A2. Observed and simulated 5% damped response spectra for the 1988 Saguenay foreshock (solid and dashed lines, respectively). Stations are arranged in the order of increasing hypocentral distance. Station name and hypocentral distance in kilometers appear on top of each plot. Observations and simulations are compared at frequencies of 1, 2, 5, and 10 Hz, where observed data are available.

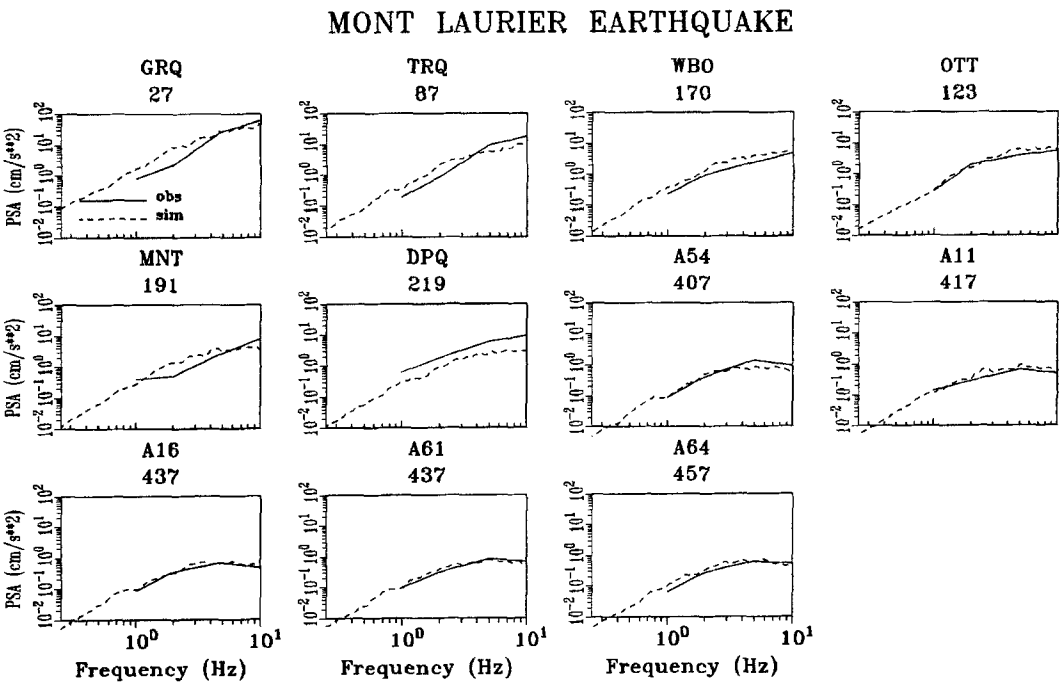

Figure A3. Observed and simulated 5% damped response spectra for the 1990 Mont Laurier earthquake (solid and dashed lines, respectively). Stations are arranged in the order of increasing hypocentral distance. Station name and hypocentral distance in kilometers appear on top of each plot. Observations and simulations are compared at frequencies of 1, 2, 5, and 10 Hz, where observed data are available.

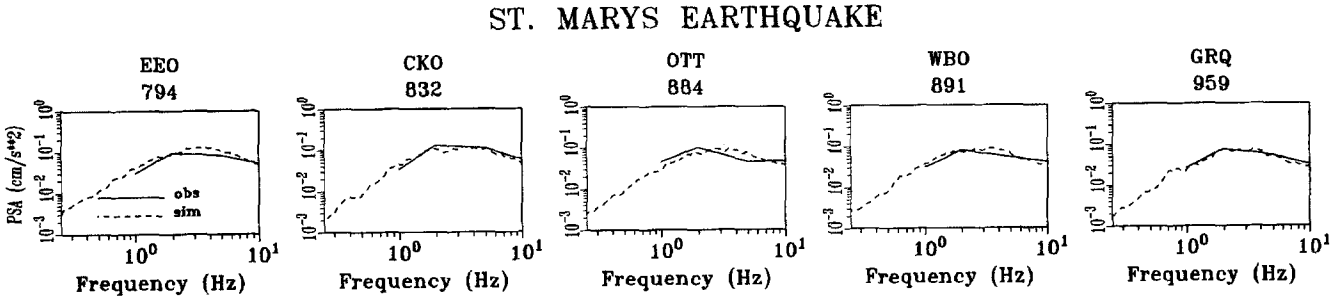

Figure A4. Observed and simulated 5% damped response spectra for the 1986 St. Marys earthquake (solid and dashed lines, respectively). Stations are arranged in the order of increasing hypocentral distance. Station name and hypocentral distance in kilometers appear on top of each plot. Observations and simulations are compared at frequencies of 1, 2, 5, and 10 Hz, where observed data are available.

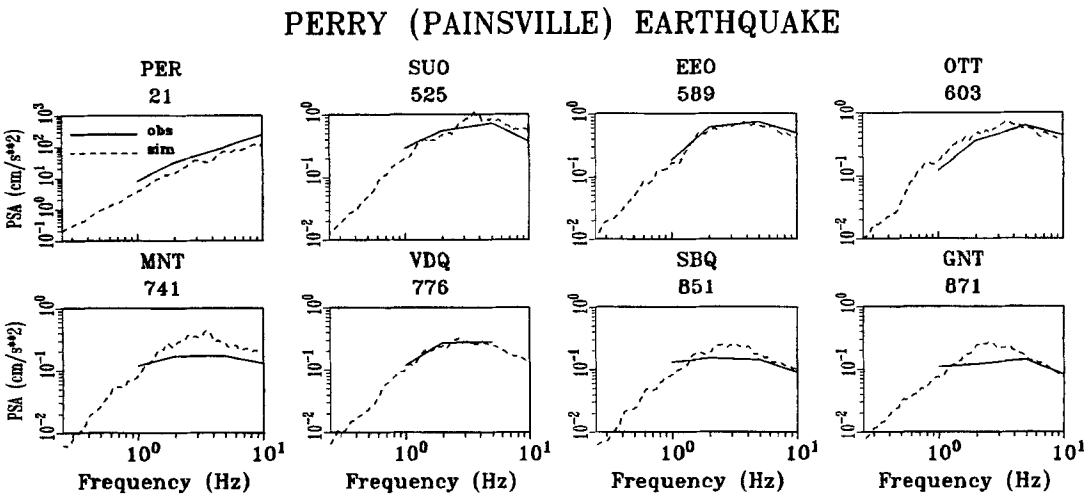

Figure A5. Observed and simulated 5% damped response spectra for the 1986 Perry (Painsville) earthquake (solid and dashed lines, respectively). Stations are arranged in the order of increasing hypocentral distance. Station name and hypocentral distance in kilometers appear on top of each plot. Observations and simulations are compared at frequencies of 1, 2, 5, and 10 Hz, where observed data are available.

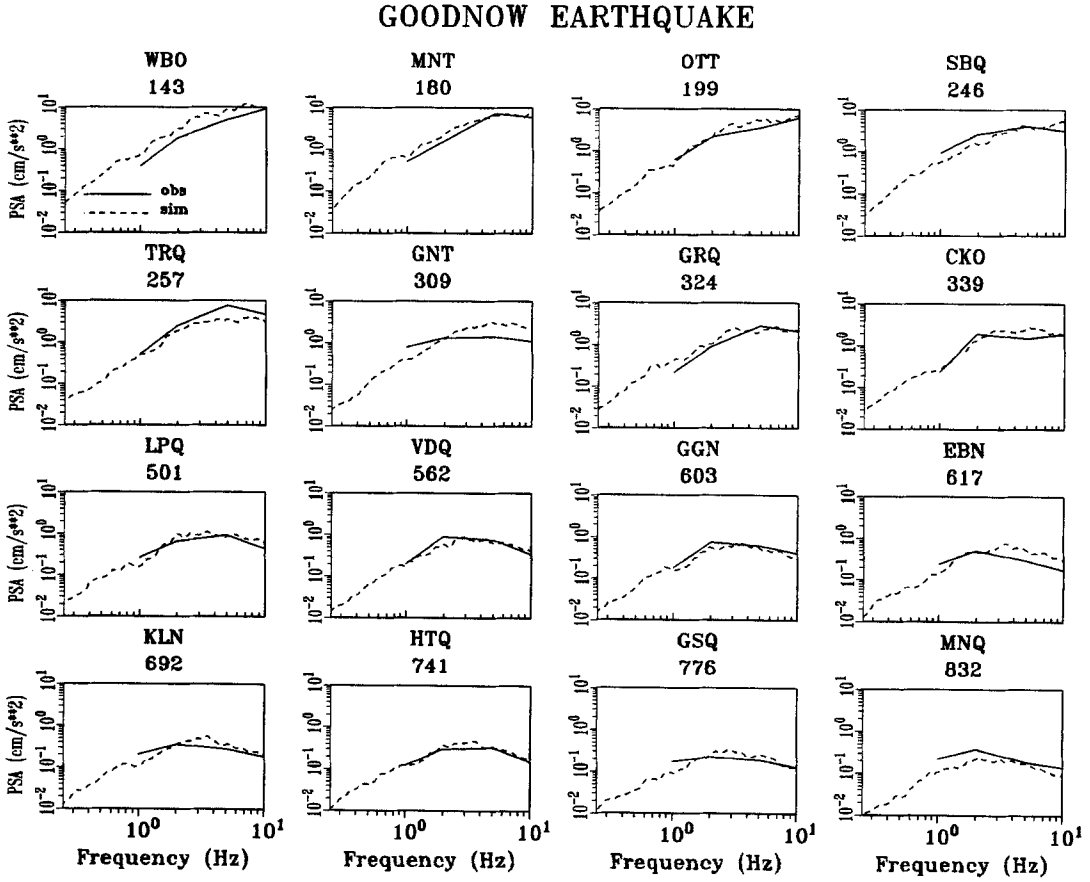

Figure A6. Observed and simulated 5% damped response spectra for the 1983 Goodnow earthquake (solid and dashed lines, respectively). Stations are arranged in the order of increasing hypocentral distance. Station name and hypocentral distance in kilometers appear on top of each plot. Observations and simulations are compared at frequencies of 1, 2, 5, and 10 Hz, where observed data are available.

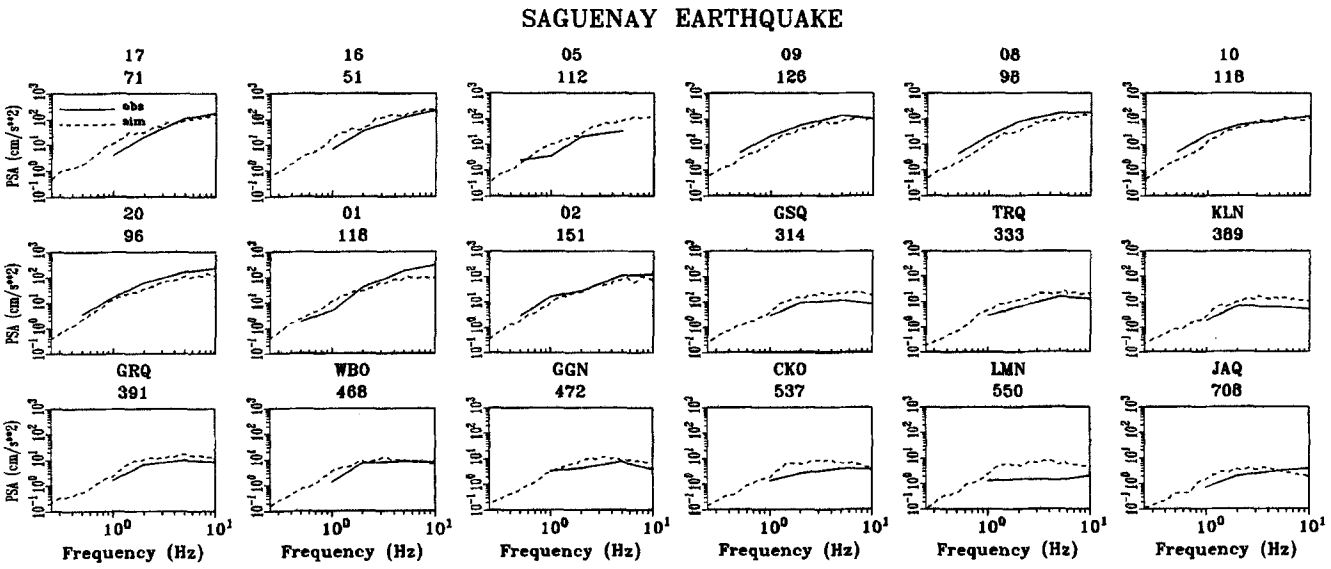

Figure A7. Observed and simulated 5% damped response spectra for the 1988 Saguenay mainshock (solid and dashed lines, respectively). Strong-motion stations (17 to 02) are shown first, clockwise from northwest direction (see text). Strong-motion stations are followed by regional stations, arranged in the order of increasing hypocentral distance. Station name and hypocentral distance in kilometers appear on top of each plot. Observations and simulations are compared at frequencies of 0.5, 1, 2, 5, and 10 Hz, or where observed data are available.

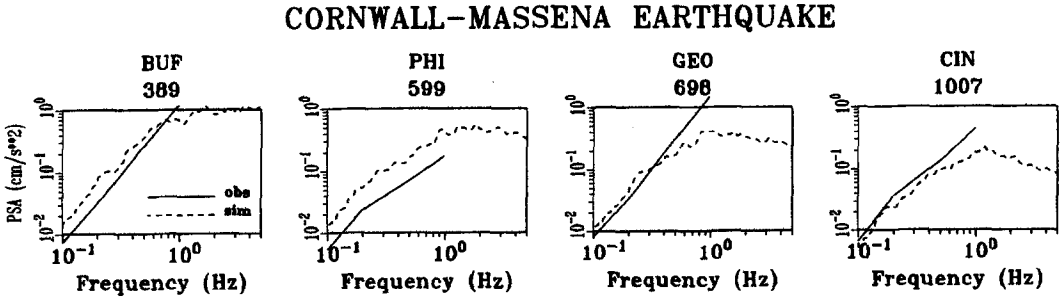

Figure A8. Observed and simulated 5% damped response spectra for the 1944 Cornwall-Massena earthquake (solid and dashed lines, respectively). Stations are arranged in the order of increasing hypocentral distance. Station name and hypocentral distance in kilometers appear on top of each plot. Observations and simulations are compared at frequencies of 0.1, 0.2, 0.5, and 1 Hz, where observed data are available.

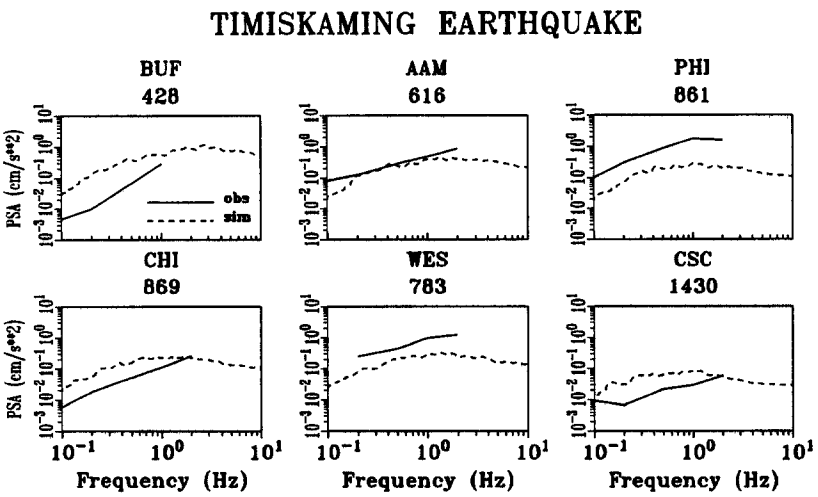

Figure A9. Observed and simulated 5% damped response spectra for the 1935 Timiskaming earthquake (solid and dashed lines, respectively). Stations are arranged in the order of increasing hypocentral distance. Station name and hypocentral distance in kilometers appear on top of each plot. Observations and simulations are compared at frequencies of 0.1, 0.2, 0.5, 1, and 2 Hz, where observed data are available.

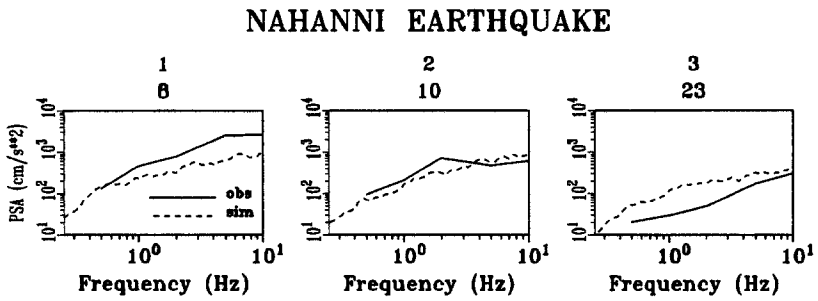

Figure A10. Observed and simulated 5% damped response spectra for the 1985 Nahanni mainshock (solid and dashed lines, respectively). Stations are arranged in the order of increasing hypocentral distance. Station name and hypocentral distance in kilometers appear on top of each plot. Observations and simulations are compared at frequencies of 0.5, 1, 2, 5, and 10 Hz, where observed data are available.

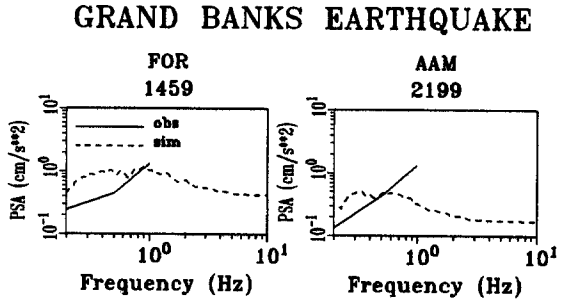

Figure A11. Observed and simulated 5% damped response spectra for the 1929 Grand Banks earthquake (solid and dashed lines, respectively). Stations are arranged in the order of increasing hypocentral distance. Station name and hypocentral distance in kilometers appear on top of each plot. Observations and simulations are compared at frequencies of 0.2, 0.5, and 1 Hz, where observed data are available.